FINAL PUBLISHABLE REPORT

Grant Agreement number	20FUN04
Project short name	PrimA-LTD
Project full title	Towards new primary activity standardisation methods based on low-temperature detectors

Project start date and duration:		01 June 2021, 36 months	
Coordinator: Ole Jens Nähle, PTB Tel: +49 531 592 6110 E-mail: ole.j.naehle@ptb.de			
Project website address: https://prima-ltd.net/			
Internal Funded Partners: 1. PTB, Germany 2. CEA, France 3. CHUV, Switzerland 4. CIEMAT, Spain	External Funded Partners: 5. CNRS, France 6. IPSA, France 7. JGU, Germany 8. KIT, Germany 9. UHEI, Germany 10. UNL, Portugal	Unfunded Partners:	
RMG: -			

Report Status: PU Public

This publication reflects only the author's view and the Commission is not responsible for any use that may be made of the information it contains.

EMPIR

EURAMET

The EMPIR initiative is co-funded by the European Union's Horizon 2020 research and innovation programme and the EMPIR Participating States

Final Publishable Report

- 1 of 23 -

TABLE OF CONTENTS

1 Overview

Radionuclide metrology, and more specifically, activity standardisation, is based on well-established measurement techniques that have been used and improved for decades. However, some nuclides such as the α-decaying ^{241}Am, show better achievable uncertainty compared to e.g., ^{55}Fe, that decays by low-energy electron capture (EC). New techniques for activity standardisation using low-temperature calorimeters, namely magnetic microcalorimeter (MMC) were developed defining the starting point of future radionuclide metrology closing the uncertainty gap. The combination of high-resolution decay energy spectrometry (DES) for radioactive decays with sophisticated novel theoretical calculations of the spectrum shape increased our knowledge of fundamental decay data and processes.

In this project, new MMC detectors and associated source preparation techniques were developed and their capability for ultra-high-resolution spectrometry was experimentally demonstrated. In addition, theoretical calculation methods for beta decay and complex electron-capture processes were significantly improved. The experimental results as well as the new calculation methods will help researchers in many disciplines such as radionuclide metrology and nuclear medicine. The use of MMCs for primary activity standardization proved to be very difficult and requires further research and developments.

2 Need

The composition of radioactive sources used in industry, or for nuclear medicine is challenging to determine. NMIs and DIs follow the ever-changing and increasing demands of emerging radionuclides since each new entrant requires a specifically adapted standardisation procedure. This is important for low-energetic decays since their strong model dependence makes standardisation difficult, resulting in high uncertainties. A solution to this problem is to employ Low Temperature Detectors (LTDs) due to extremely low energy thresholds (down to a few 10 eV) and applicability to all types of nuclear decays. Hence, LTDs offer the possibility to be used as a universal tool for activity standardisation.

The second pillar of radionuclide metrology is the determination of nuclear decay data. The most effective way to accurately determine decay data is to use recently developed theoretical models. Although the newer models include more detailed effects of the underlying nuclear and atomic physics, they still do not cover all types of decays, for example the second forbidden non-unique decay of ^{129}I. Additionally, the theory needs accurate experimental data for validation. LTDs can deliver validation data obtained from high-resolution, high statistics measurements in 4π geometry.

3 Objectives

The overall objective of the project was to improve the capabilities in radionuclide metrology, by developing a new primary activity standardisation method based on low temperature detectors and improving on fundamental nuclear decay data.

The specific objectives of the project were:

1. To develop a new primary method for decay scheme independent activity determination using low temperature detector-based spectrometers with a quantum efficiency of 100 %, high energy resolution and with the capability of processing measurement statistics which exceed 10^8 events / spectrum.

2. To combine new source preparation techniques (e.g., ion-implantation), and modern detectors (e.g., metallic magnetic calorimeters, etc.), in order to standardise one α emitter (^{241}Am), one β emitter (^{129}I) and one electron-capture nuclide (^{55}Fe). This aimed to considerably reduce the uncertainty compared to existing methods.

3. To develop a method for the measurement of ^{55}Fe energy spectra with a better energy resolution and a lower energy threshold (< 50 eV) than existing techniques, to be used to determine fractional electron-capture probabilities. This included determining L-subshell probabilities and a precise study of shake-up and shake-off effects. In addition, this approach was used to determine the beta spectrum shape of ^{129}I down to 0 keV.

4. To compute beta spectrum shapes and electron-capture decay using new calculation techniques, which consider all relevant effects from atomic and nuclear structure.

5. To facilitate the take up of the technology and measurement infrastructure developed in the project by the measurement supply chain (NMIs, DIs, research laboratories) and users (authorities with responsibilities in radiation protection and environmental monitoring, researchers in allied fields).

4 Results

These are the results of joint collaborative work.

4.1 Objective 1: Development for the application of advanced MMC detectors for radionuclide spectrometry and activity standardisation

The MMC detectors developed by KIT with support from UHEI within *PrimA-LTD* were conceptualized and dimensioned to perform activity standardisation of the α-decaying isotope [241]Am, the β-decaying isotope [129]I and the electron-capture (EC) decaying isotope [55]Fe with much improved uncertainties compared to conventional measurement techniques. Two detector types have been designed and fabricated. The first type (called RoS, for **R**eusable **o**r **S**ingle-use) was designed for demonstrating activity standardisation on the above-mentioned nuclides, that are embedded in absorbers, prepared separately from the detectors. Choosing an absorber with suitable thickness for each radionuclide ensures a detection efficiency very close to 100%, which is a key requirement for absolute activity measurements. In past applications using MMCs in radionuclide metrology, such absorbers were glued directly and permanently onto the paramagnetic sensor. This way, standardisation measurements performed on a regular basis are cost- and resource-intensive as for each measurement a detector has to be fabricated. Therefore, a key feature of the RoS detector type is the reusable operation option by allowing for gold wire-bond contacts between the absorber/source composite and the MMC. A single detector chip can be reused for multiple measurements by replacing the connected absorber/source composite.

As the above-mentioned radionuclides have different decay energies, the required absorber thickness varies from nuclide to nuclide and was defined for each by radiation transport simulations at CEA. Generally, to ensure optimal detector performance, the detector's total heat capacity needs to be minimized, resulting in different absorber heat capacities for each radionuclide. For this reason, two RoS design variants were developed, the RoS-L variant being optimized for measuring [241]Am and [129]I and the RoS-M variant for [55]Fe. The design process of a detector design takes the absorber heat capacity as a starting point and from there finds a detector geometry optimized to achieve best possible energy resolution. For this, complex numerical simulations of the MMC operation and performance were carried out. The results of the detector optimizations are summarized in *Table 1.*

Table 1 Optimized detector properties of the all detectors developed within *PrimA-LTD* at an operating temperature of 20 mK. An erbium concentration of 475 ppm in the Ag:Er temperature sensor was assumed.

Detector type	RoS-L	RoS-M	Implanted [55]Fe detector
Absorber heat capacity	400 pJ/K	110 pJ/K	1 pJ/K
Sensor heat capacity	297 pJ/K	71 pJ/K	1 pJ/K
Sensor size (area · thickness)	(1015 µm)² · 3 µm	(495 µm)² · 3 µm	(135 µm)² · 0.5 µm
Single pixel inductance	28.5 nH	6.79 nH	0.92 nH
Expected ΔE_{FWHM}	38.5 eV	19.5 eV	2.1 eV

The optimized detector geometries were transferred into a technical layout and are depicted for both RoS variants in *Figure 1.* Both detectors comprise two pixels that are connected in parallel and that each have a Ag:Er layer placed on top of a superconducting pick-up coil made from niobium. The persistent current is prepared by the use of a persistent current switch, that is placed between the pixels. The pixels are arranged in an almost gradiometric configuration, meaning that the size of the right pixel is reduced to 95% compared to the left pixel. In this way, global temperature fluctuations affecting both pixels lead to a baseline shift in the readout-SQUID, which enables monitoring of heat bath temperature variations. The pixels are equipped with dedicated bond pads, to which external absorbers can be wire-bonded. These pads as well as the whole sensor area is entirely covered with a highly conductive, 3 µm thick electroplated gold layer that ensures a homogeneous heat transfer from the bonding areas to the temperature sensor. In addition, stems are provided on the sensor area that allow for conventional gluing of the absorber directly onto the sensor. Each pixel is connected to its own on-chip heat bath by a gold strip, the thermal conductivity of which is designed to obtain

a signal decay time of about 1 ms. Bond pads, to which the readout-SQUID can be connected, are available at the lower edge of the chip.
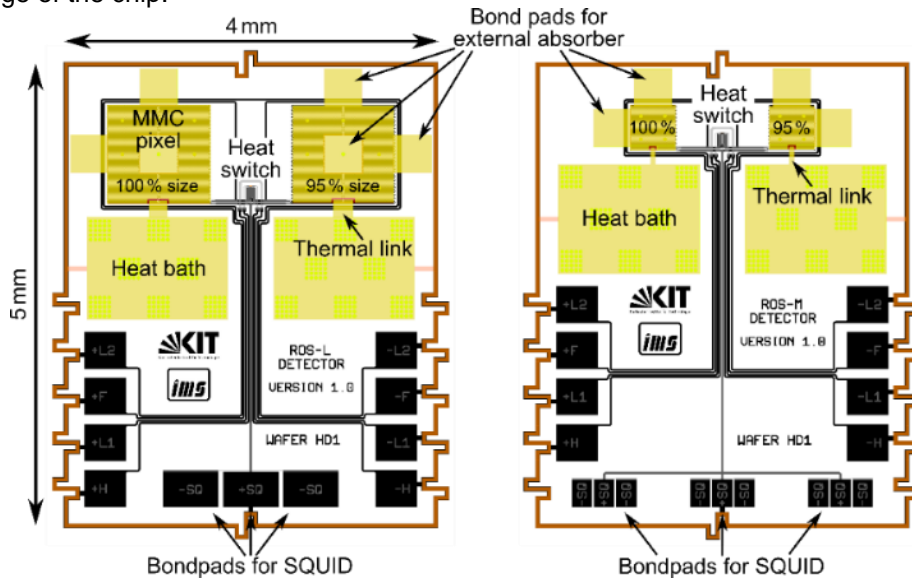

Figure 1: Chip designs of the RoS-L (left) and RoS-M (right) detectors for activity standardisation using MMCs.

The microfabrication of both RoS detector designs was performed in the same procedure on one 3-inch silicon wafer coated with a SiO_2 layer of about 250 nm thickness. With this, a total of 140 RoS-L and 36 RoS-M chips were fabricated. The sequence of the different layers fabricated is listed in *Table 2*.

Table 2 Individual fabrication steps for RoS type detectors.

Layer	Material and aimed thickness	Process
1	Nb, 250 nm	Sputter deposition followed by UV-photolithography with positive-tone photoresist and reactive ion etching
2	Nb_2O_5	Anodic oxidation of first Nb layer using a resist mask created by negative-tone photoresist
3	SiO_2, 175 nm	UV-Photolithography with negative-tone photoresist followed by sputter deposition
4	SiO_2, 175 nm	UV-Photolithography with negative-tone photoresist followed by sputter deposition
5	AuPd	UV-Photolithography with negative-tone photoresist followed by sputter deposition
6	Nb, 600 nm	UV-Photolithography with negative-tone photoresist followed by sputter deposition
7	Ag:Er + 100 nm Au	UV-Photolithography with negative-tone photoresist followed by sputter deposition
8	Au, 400 nm	UV-Photolithography with negative-tone photoresist followed by sputter deposition
9	Au, 3 μm	UV-Photolithography with positive-tone photoresist followed by electroplating
10	Au, 3 μm	UV-Photolithography with positive-tone photoresist followed by electroplating

Table 3 Extra fabrication steps for the microfabrication of the implanted ^{55}Fe detector.

Layer	Material and aimed thickness	Process
9	Au, 12 μm	UV-Photolithography with two positive-tone photoresist layers followed by electroplating
10	^{55}Fe	UV-Photolithography with positive-tone photoresist followed by ion-implantation
11	Au, 12 μm	UV-Photolithography with positive-tone photoresist followed by electroplating

The second detector type, named implanted ^{55}Fe detector, was designed for measuring the decay energy spectrum of the nuclide ^{55}Fe with the best possible energy resolution, high statistics with ~10^8 counts as well as 99.99% detection efficiency for photon energies <6.5 keV. To achieve this detection efficiency, a gold absorber thickness of 12 μm is required. A novelty in the field of radionuclide metrology is the integration of the ^{55}Fe source into the absorber by ion-implantation. In this way, no source induced spectral distortions are to be expected that worsen the achievable energy resolution. The detector optimization for this type was carried out similarly as for the RoS type detectors. Due to the comparably small energies to be detected, the result was a much smaller optimal geometry compared to the RoS detectors. The results of the optimization are summarized in *Table 3*.
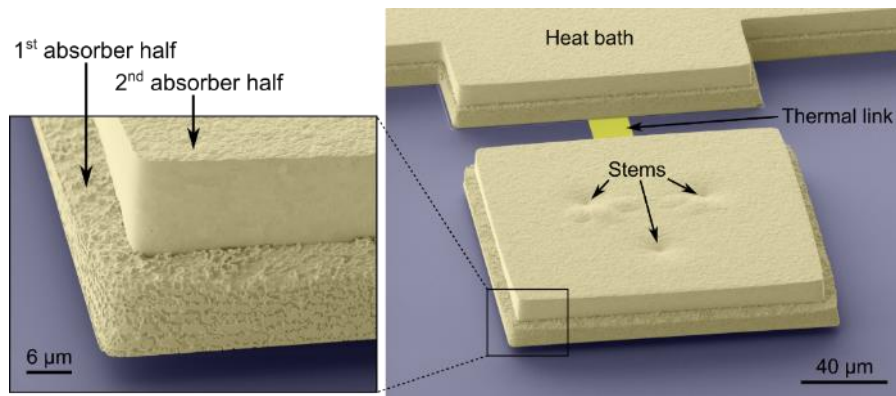

Figure 2: Colorized SEM image of a fully microfabricated free-standing 4π particle absorber made of two separately electroplated gold layers with 12 μm of thickness each.

Integration of the source in 4π geometry in the comparably small (170 μm)² absorbers required a complex three-step microfabrication process: i) deposition of the first absorber half, ii) ion-implantation of ^{55}Fe into the first absorber half and iii) deposition of the second absorber half. For optimal detector performance, the absorber needs to be made of highly conductive gold fabricated by electroplating of the gold with plating parameters that allow for the growth of highly pure, crystalline gold films. Furthermore, the absorber needs to be free-standing on a few small stems to prevent energy loss in the early stage of absorber thermalization. This microfabrication process was successfully developed and demonstrated for the first time within *PrimA-LTD. Figure 2* shows a colorized SEM image of such an integrated 4π absorber.

The ion-implantation was carried out on chips as depicted in *Figure 3.* They contain a total of 16 individual detectors with 32 pixels, 20 of which are to be implanted. The pixels are arranged in straight line, to allow for a straight ion-implantation path. Contact pads on the very left and right are used for electroplating of the second absorber half. After completed fabrication, the chip can be used as is or further diced in up to 4 single sub-chips. The bond pad configuration for providing field and heater currents is similar to the RoS detector designs. The layer sequence is for the most part identical to the RoS detector fabrication. Exceptions are, that layer 7 and 8 were switched and that from layer 9 the process steps listed in *Table 3* were performed for the microfabrication of the absorbers. The fabrication took place on 2-inch silicon wafers that were covered with a 250 nm thick SiO$_2$ layer. Each wafer contained a total of eight chips as depicted in *Figure 3.*
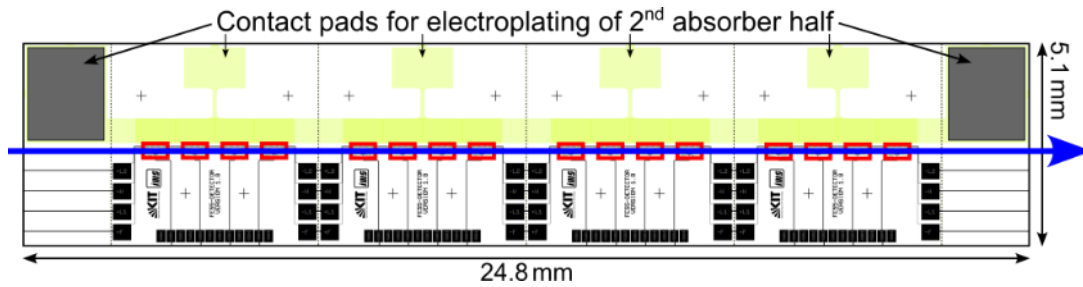
Figure 3: Design of an implanted ^{55}Fe detector chip to be ion-implanted with ^{55}Fe. The positions of the individual detector pixels are indicated by red boxes. The ion-implantation path is indicated by a blue arrow.

The advanced MMC detectors developed within *PrimA-LTD* have been used by the consortium partners CEA and PTB. To do so, both their spectrometer set-ups have been significantly upgraded. The number of readout channels has been extended from two channels at the project start to more than 10. Novel detector modules were conceptualized, fabricated and tested. Correspondingly, data acquisition hardware and software components to enable multi-channel MMC/SQUID readout have been successfully integrated into both set-ups. These extensions result in a reduction of the required spectrometer operation time by a factor of 5 or more when performing measurements. This way, high statistics measurement with 10^8 events per spectrum are now feasible with both spectrometers in reasonable times. The novel detector modules were adapted to the millikelvin refrigerators operated at CEA and PTB, respectively. For the CEA set-up, the detector module can hold up to 10 MMC and SQUID chips and is designed to fit into a relatively narrow experimental space (diameter 90 mm). It is a fully modular configuration (*Figure 4),* where each individual MMC and SQUID chip is placed on an individual platelet mounted to the support structure. The electrical connections for the field current and heater current to the MMCs can be connected in series ("daisy chaining"); small PCBs for this chip-to-chip connection are placed between the MMC chips. The set-up can be completed by a calibration source and collimator plate placed above the MMCs and absorbers. Different plates can be prepared with different aperture diameters according to the absorber size and the calibration source activity. Individual calibration sources can be placed above each pair of apertures, such that even different radionuclides can be used as calibration sources if required. The MMC / absorber-to-collimator distance can be varied by spacers of different height. The new CEA detector module greatly simplifies changing or adding individual MMC detector chips in a reliable manner.
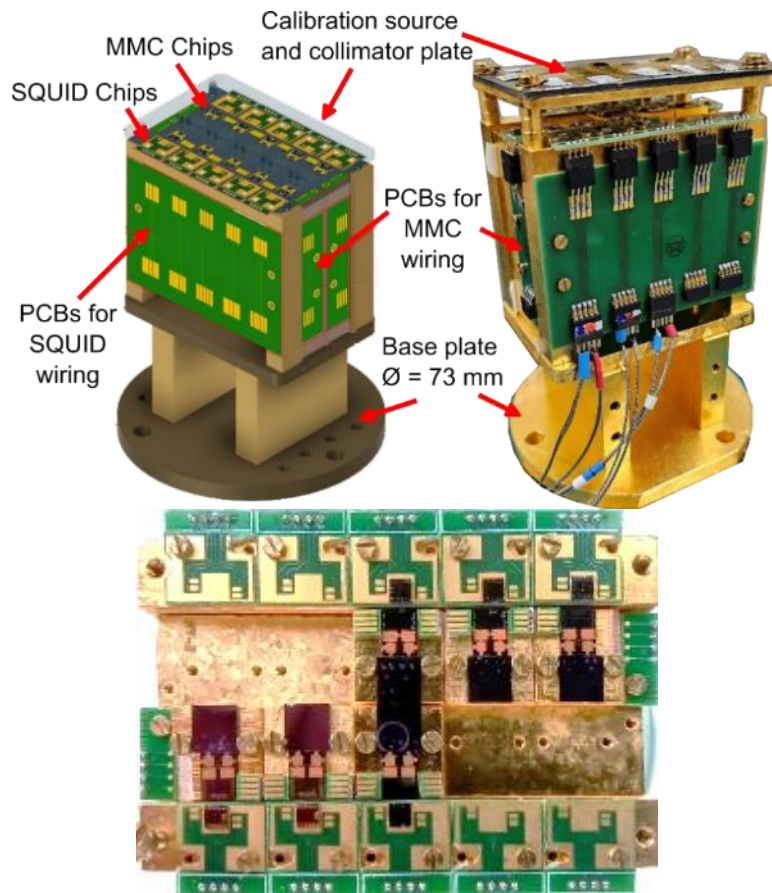
Figure 4: Top: 10-channel MMC detector module for CEA spectrometer with calibration source/collimator plate. Bottom: Top view of the module without collimator plate and 6 mounted MMC/SQUID pairs.
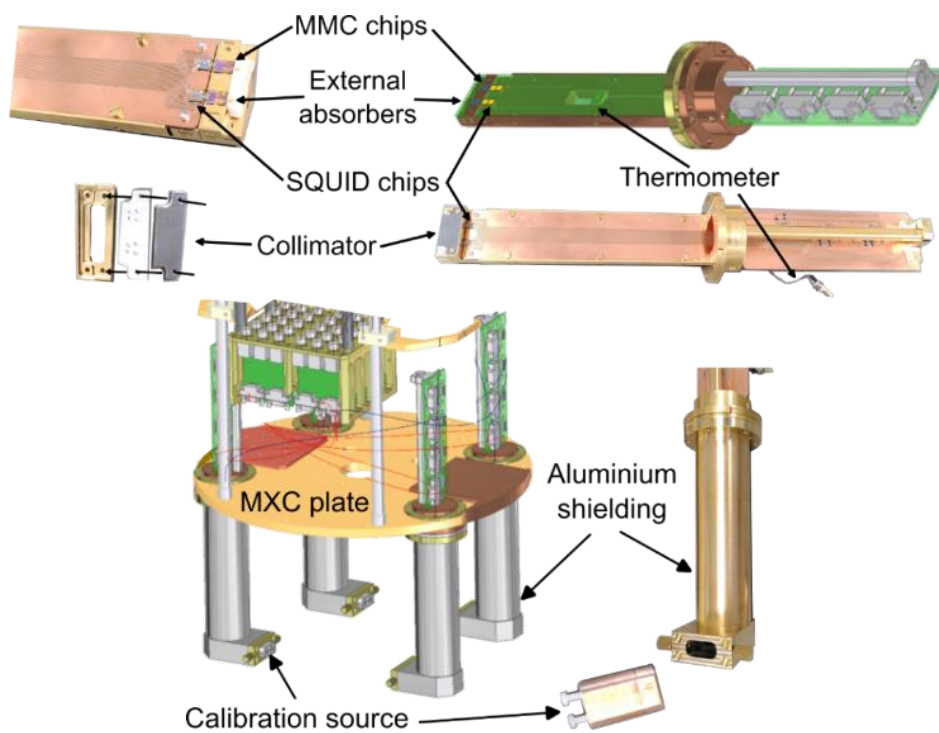

Figure 5: MMC detector modules for PTB spectrometer with superconducting magnetic shields and their arrangement on the mixing chamber plate of the millikelvin refrigerator of the PTB system.

The new detector modules for the PTB spectrometer and their configuration are show in *Figure 5*. Given the larger experimental volume of the PTB setup's millikelvin refrigerator, the modules have been designed and realised such that up to 4 can be operated in one cooldown. The modules comprise a half-spherical metal base body from thermally annealed copper, onto which metal platelets that hold the SQUID and MMC chips are placed on. Parasitic thermal loading of the MMCs by the power dissipation in the nearby SQUID sensors, is minimized in the chosen configuration. The modules are compatible with the reusable MMCs detector developed within *PrimA-LTD* for external source/absorber elements. These elements can be placed on a separate carrier next to the MMC detector chips and thermally connected by means of gold wires. The modules are prepared for a resistive thermometer in a standard housing to be mounted on the base body. Custom PCBs, made from low-temperature compatible phenoplast, are used to provide electrical connections to the MMC detector and SQUID sensor chips by means of ultrasonic wire bonding from pads on the PCBs to pads on the detector and sensor chips. The modules are connectorized using commercial MWDM-15 socket connectors. Correspondingly connectorized wiring harnesses are used for the electrical connections to the room-temperature electronics. The body of each individual detector module is placed inside a superconducting magnetic shielding made of aluminium. Integrated in the shields are positions for external X-ray- or gamma ray calibration sources. Their distance and, hence, the rate of photons from the calibration sources that reach the detectors is adjustable. Four modules can be mounted onto the 10 mK plate of the dilution refrigerator operated at PTB. In this configuration up to 16 MMC/SQUID readout channels are available simultaneously.

In summary, novel MMC detectors were developed and fabricated at KIT, with UHEI supporting the fabrication. The two MMC types were optimized for decay energy spectrometry of ^{55}Fe and for activity standardisation measurements of various radionuclides. The MMCs were characterized at KIT, PTB and CEA confirming the functionality. The spectrometers at CEA and PTB were upgraded allowing multichannel MMC operations. As a result, the objective was fully satisfied.

4.2   Objective 2: Radioactive source preparation and primary activity standardisation

New source preparation techniques needed to be explored to enable fabrication of samples suitable for MMC measurements as well as for primary and secondary activity measurements using established methods and detectors. Such samples were needed for validation purposes of the newly developed activity determination methods using MMC. In addition, the used source preparation technique strongly affects the quality of measured decay energy spectra. For highest spectral quality without any spectral distortions, ion-implanted sources were created for decay energy spectrometry. In this section, we will highlight the progress achieved in source preparation and in development of activity determination methods using MMCs including the comparison and validation with established techniques.

A comprehensive investigation into various production methods for radioactive sources, in particular ^{55}Fe, ^{129}I and ^{241}Am was undertaken. The objective was to develop sources suitable for primary activity standardisation (Objective 2) and high-resolution decay energy spectrometry (Objective 3).

The initial focus was on developing nanostructured absorber surfaces that could be integrated with the geometry of MMC detectors developed as described in Section 4.1. Compared to non-nanostructured absorbers, two enhancements were expected. Firstly, the effective area for drop deposition increases, enabling the deposition of a higher ratio of activity and number of atoms of the radionuclide on absorbers with the same dimensions. This is especially important for the very long-lived nuclide ^{129}I. And secondly, potential saline residuals are reduced, which are created after the activity-containing aqueous solution dries up. Thus, non-detected decay energy loss due to the occurrence of these residuals can be minimized and a clean decay energy spectrum can be measured. These nanostructured surfaces were created through a process of co-sputtering alloys followed by selective etching to remove unnecessary alloy components. Specifically, for ^{241}Am sources, nanostructured gold surfaces were produced by applying an Au-Ag alloy and then etching away the silver component using nitric acid. Similarly, for ^{129}I sources, nanostructured silver surfaces were fabricated by applying an Ag-Al alloy and subsequently etching away the aluminium component using hydrochloric acid. This development work was carried out at C2N. Both processes were optimized during the project and yielded absorbers of the required quality (compare to *Figure 6*).
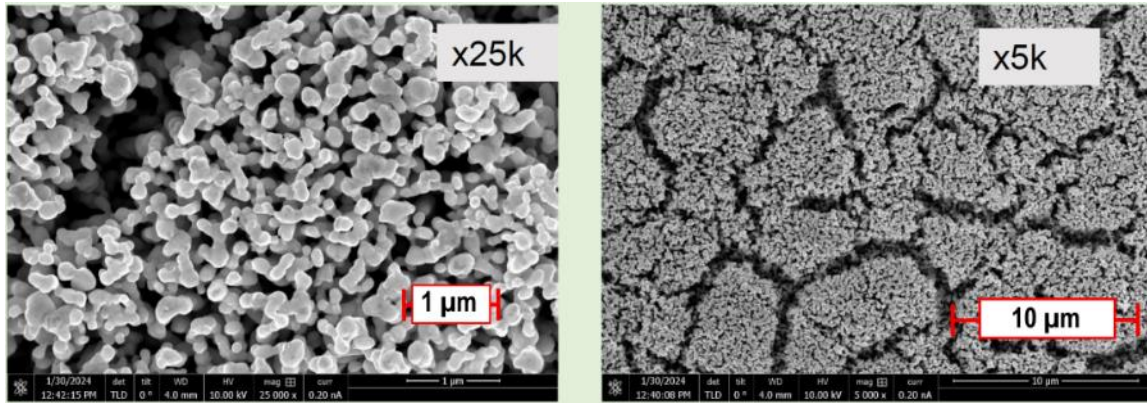
Figure 6: SEM images of a silver nanofoam with a thickness of 2.8 µm and 2.4 mm diameter. Left: 25k magnification. Right: 5k magnification. No crystalline structures caused by aluminium and oxygen residuals are left.

Micro-dispensing techniques were also explored as a new quantitative method to produce high-quality radioactive sources. Experiments with ^{241}Am solutions were conducted at LNHB and with ^{55}Fe at PTB. The core idea was to determine the exact mass of solution applied to an absorber using a micro-dispenser by precisely weighing a reservoir. However, this technique proved to be insufficiently precise due to several issues. A significant source of error was the loss of volume from the reservoir due to evaporation during the waiting period. Additionally, the technique suffered from non-reproducibility when large numbers of droplets were applied successively using the dispenser. Consequently, micro-dispensers were deemed unsuitable for quantitative source production within the project frame. Meanwhile, NIST (not involved in this project) developed a weighing routine for similar small amounts of deposited solutions by weighing the reservoir and reference weights multiple times. In future works, this routine could also be applied here. At PTB a semi-quantitative approach of source preparation was examined. Instead of weighing, the number of dispensed and deposited droplets were used as reference. By creating samples suitable for liquid scintillation counting in parallel to each MMC sample, a reference link to an established method was created (see *Figure 7* right). In order to study the stability and reproducibility of the micro-dispensing system, several samples for liquid scintillation counting (LSC) were prepared and analysed. As a result, the deposited activity per volume varies by approximately 2% from each other by dispensing the same number of droplets.
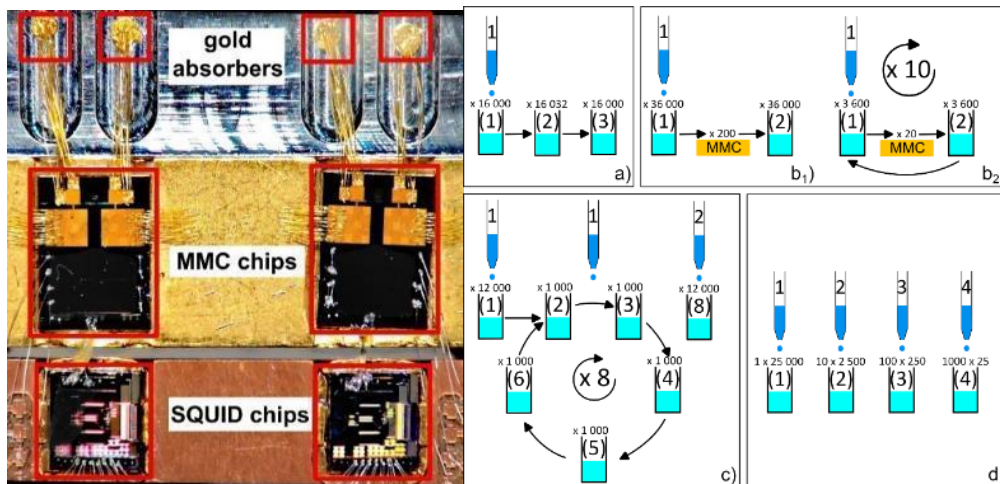

Figure 7: Left: Photography of a MMC setup containing external ^{55}Fe micro-drop deposited samples of 100 µm thick and 680 µm in diameter gold absorbers. Right: Micro-dispensing routines for preparing LSC and MMCs samples used to investigate on the reproducibility of the system.

The deposited activities in the LSC samples were determined using the triple-to-double coincidence ratio (TDCR) method. The TDCR method is well-established in radionuclide metrology and makes use of detector systems with three photomultiplier tubes (PMT). In case of the MMC method, a software trigger based on a RC-CR2 filter and an extended deadtime was used. After micro-drop deposition, the MMC samples were

enclosed with a second gold foil by diffusion welding. The fully prepared samples were then attached to the MMCs using gold wire bonds (*Figure 7* left). The determined activity of the samples by using the MMC method were up to 20% higher than expected from the LSC measurements. This could be due to the comparison of samples prepared by depositing a small number of droplets, less than 200 for the MMC samples, with samples prepared by dispensing 30 000 droplets. We observed that the discrepancy between MMC and LSC measurements becomes lower (up to 1%) if more droplets are dispensed at once in the MMC samples. Resulting, the increase in activity seemed to be caused by the preparation routine.

For ^{129}I source production, a straightforward immersion process was implemented at LNHB. The previously produced nanostructured silver absorbers were immersed in an ^{129}I solution, where the high chemical affinity of iodine to silver facilitated sufficient ^{129}I activity via self-adsorption. The quality of these absorbers was monitored using radiography and gamma-ray spectrometry (compare to *Figure 8*).
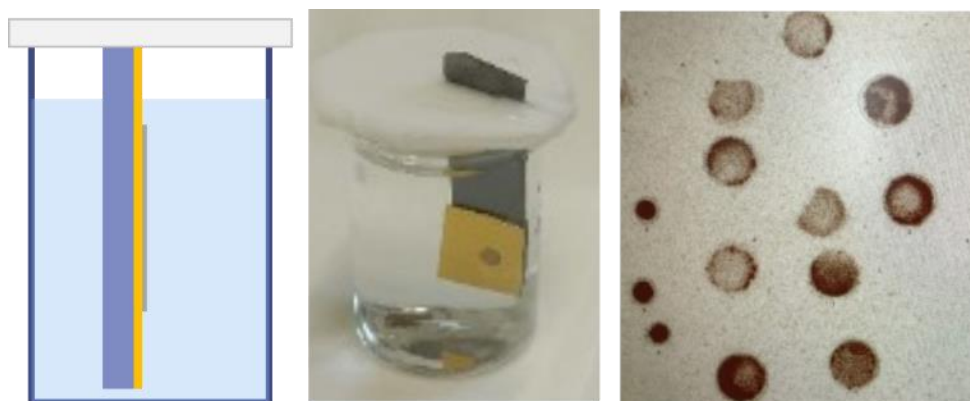

Figure 8: Left: schematic view of ^{129}I source preparation. The sample consists of 3 µm thick NPAg layer (gray) on top of 20 µm thick gold layer (gold) which is on top of silicon substrate (purple) with a thickness of 250 µm. The source is dipped in a solution containing ^{129}I. Middle: Image of ^{129}I source preparation. Right: Autoradiography of radioactive samples.

The ^{129}I sources were placed in between two gold foils and diffusion welded to form a 4π absorber. The actual measurement setup will be further discussed in Section 4.3. Because iodine is very volatilising, no direct link between MMC measurements and established methods could be established for ^{129}I. Nevertheless, the activities of the ^{129}I sources were roughly determined by gamma-ray spectrometry. The MMC-based method used a software trigger by applying a narrow bandpass filter and a leading-edge discriminator. The live time is determined using an extended deadtime algorithm. The determined activity agreed with the activity obtained by the gamma spectrometry measurements.

To produce ^{241}Am sources for MMC measurements, the electrochemical deposition method was selected. This involved depositing ^{241}Am on nanostructured gold absorbers. Initially, a large, masked area was deposited at LNHB, which was then segmented into smaller units suitable for MMC geometry (see *Figure 9*). Two types of masked were tested, one consisting of a copper tape and the other made of Kapton. Quality control of the individual absorbers was conducted using radiography and alpha spectrometry measurements, with the most suitable absorbers selected based on the desired activity.
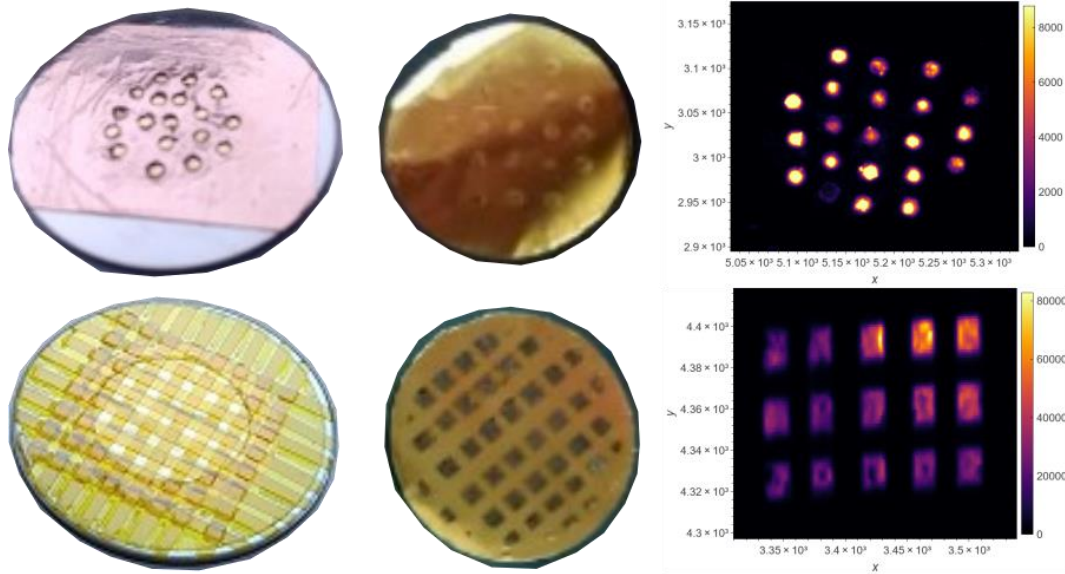
Figure 9: Images of ^{241}Am sources prepared by using a mask made of copper tape (top row) and of Kapton (bottom row) Left: The masked samples before electro-precipitation of ^{241}Am. Middle: The sources after electro-precipitation and removal of masks. Right: Autoradiography images of the sources.

After preparation of the open alpha-decaying ^{241}Am sources at LNHB, they were sent to each NMI/DI partner for activity determination. Different measurement techniques were applied: measurements in ionization chambers (IC), defined solid angle measurements (DSA) and coincidence counting measurements (CC). The activity of the samples was first determined at LNHB by DSA measurements. Afterwards, they were sent to CIEMAT where measurements were performed using an ionization chamber with a grid, an alpha-gamma coincidence counter consisting of a pressurized proportional counter and a NaI(Tl) detector, and a DSA detector. Then, the activities of the samples were determined at CHUV using a DSA silicon detector and finally measurements were performed at PTB with a 4π proportional counter and NaI(Tl) coincidence system. The results of one of these intercomparisons is shown in *Figure 10*. Besides the uncommon sample geometry and low activity, the results agreed with each other. The samples were sent back to LNHB, where the sample preparation was completed to create samples suitable for MMC measurements.
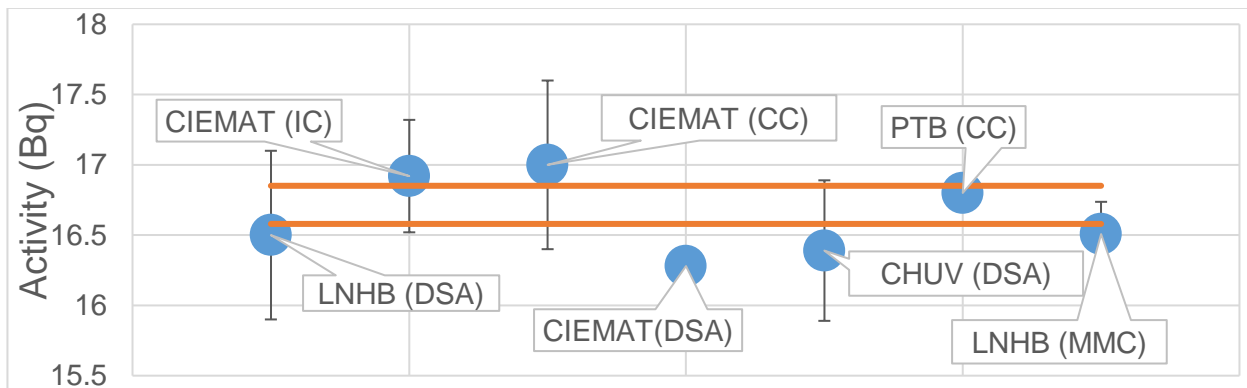

Figure 10: Comparison of determined activities of an ^{241}Am source (copper-mask) using different techniques.

The 21 ^{241}Am samples, cut-out from the sample disk prepared using the copper tape mask, were enclosed using 11 gold absorbers (multiple samples per absorber). All 11 absorbers and an additional background absorber were simultaneously measured using six RoS-L MMCs. The absorbers were attached to the MMC sensors using 25 μm diameter gold bonding wires. The analysis routine is the same as outlined in the previous paragraph concerning the ^{129}I measurements. Since the samples were cut out and not all the material of the sample disk was used for the MMC measurement, some activity in-between the cut-out pixels remained on

the disks which was lost for the MMC measurement. The autoradiography data of the corresponding sample was used to correct for this missing activity.

To produce ^{55}Fe sources for the measurement of high-quality decay energy spectra, ion-implantation techniques were employed at RISIKO off-line mass separator facility for radioisotopes operated by JGU. Based on preparative laser-spectroscopic studies on stable ^{56}Fe, a monoisotopic ^{55}Fe ion beam with the high spatial characteristics was produced to perform implantation into the array of gold absorbers. This process involves evaporating ^{55}Fe in a vacuum chamber, ionizing it through resonant laser ionization, selecting the ions with a mass separator, and finally implanting them into an absorber mounted on the focal plane. The MMC chip was mounted in and galvanically connected to a large Faraday-cup and placed behind a slit aperture (*Figure 11*). Well controlled and quantitative implantation runs were performed by strong focalization and precise positioning and scanning in X- and Y-direction of the ion beam onto the MMC chip surface. While this technique has been successfully used in other projects, such as for ^{163}Ho, it required adaptation to iron. A suitable excitation and ionization scheme was successfully developed. One anticipated challenge was the potential high concentration of ^{55}Mn in the solution, which could lower the ionization efficiency. Neutron activation analysis was used to determine the ^{55}Mn amount relative to ^{55}Fe. It was concluded that the ^{55}Mn concentration was within a manageable range, eliminating the need for additional chemical purification of the solution. Despite this, the first implantation attempt was unsuccessful, with ionization efficiency much lower than expected. The exact cause remains unclear, but improvements in the apparatus gradually increased the overall efficiency.
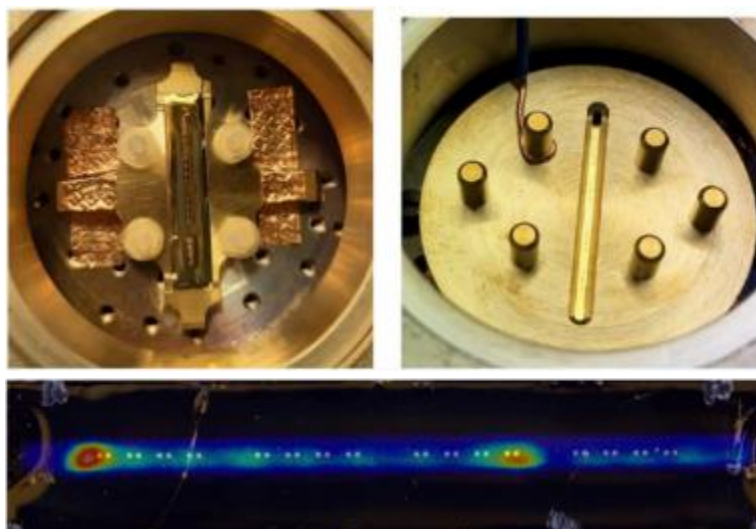

Figure 11: Implanted ^{55}Fe MMC chip mounted in the final collection Faraday cup of the RISIKO facility before and after aperture installation and optical images of the test detector chip with the implantation line indicated as well as after implantation overlayed with the activity distribution visualized by autoradiography.

The ion current on the MMC chip was read out during the implantation process. The total number of implanted atoms could then be estimated from the integration of the ion beam current measured during the entire implantation procedure of more than 2 hours. Directly following a first implantation test run, the distribution of ^{55}Fe atoms in the MMC chip was studied at PTB using autoradiography with the test chip still mounted in the irradiation holder. The result of this measurement confirmed the overall ion beam width of about 0.5 mm and a rather homogeneous deposition of activity with local 'hot spots' exceed the average activity of about 0.7 Bq per absorber by a factor of 2 to 3. Using optimized process parameters for the laser ionization, mass separation and ion beam control and quantification, subsequent implantation runs successfully achieved activities 5 Bq per absorber. This task experienced delays but ultimately, by increasing the ^{55}Fe starting activity, the desired amount of ^{55}Fe was successfully implanted in several detector chips.

To conclude, nanoporous gold and silver absorbers were developed and fabricated at CNRS. At CEA, these were further used for sample preparation of ^{241}Am source by electroprecipitation and of ^{129}I sources by self-deposition. Micodispensing techniques were exanimated at CEA and PTB. By using this technique, ^{55}Fe sources were prepared at PTB. Ion-implantation of ^{55}Fe onto MMC chips fabricated at KIT was performed at JGU by using apertures fabricated at PTB. All radioactive solutions were provided and standardised by PTB. The activity of alpha-decaying ^{241}Am samples prepared at CEA were determined using established techniques

at CEA, CIEMAT, CHUV and PTB. The corresponding results agreed with each other including the result of the MMC measurement performed at CEA. A semi-quantitative comparison of determined activities of EC-decaying ^{55}Fe samples prepared by PTB using microdrop deposition was examined at PTB. There, LSC and MMC measurements of sources prepared similar were compared. Most probably due to source fabrication, the results varied by up to 20% from each other. No feasible link between MMC activity determination measurements on beta-decaying ^{129}I samples and traditional methods were found. Supported by simulations, activities of ^{129}I samples were determined at CEA by means of MMCs. A rough comparison with gamma spectrometry performed at CEA resulted in a good agreement between the two methods. By considering the source preparation and development of activity determination methods using MMCs, the objective was fully satisfied. However, since only a direct link to established methods was found for the alpha-decaying nuclide ^{241}Am and the semi-quantitative comparison of EC-decaying ^{55}Fe resulted in large discrepancies, the objective was not fully achieved.

4.3 Objective 3: High precision measurement of ^{55}Fe and ^{129}I spectra for accurate determination of decay data

The progress within this objective was strongly affected by several delays due to unforeseen problems during MMC production and source preparation as well as long unexpected lead times of parts of the multichannel set-ups. Nevertheless, decay energy spectra of the beta-decaying nuclide ^{129}I and EC-decaying nuclide ^{55}Fe were successfully measured but with less statistics and lower quality as aimed. The measurements on ^{55}Fe were performed at PTB while the measurements on ^{129}I were performed at LNHB. The MMC/SQUID channels were readout using commercial XXF electronics from MAGNICON.

The signal processing and analysis was as followed. A continuous data stream was acquired with sampling rates of the order of 100 kS·s^{-1}. A software trigger and an extendable deadtime algorithm were applied to the data stream as mentioned in section 4.2. The resulting pulse start positions (or timestamps) were used to select pulses corresponding to a given energy calibration line. These pulses were averaged forming a template pulse. To determine the pulse amplitudes, the template pulse was least squared fitted to each pulse. This also resulted in a (reduced) χ^2 value for each pulse corresponding to the 'similarity' between pulses and template. Then, the noise (or baseline) spectrum was determined in the frequency domain. All pulses were filtered using a matched filter (also called 'optimal' filter). Energy calibration was performed by correlating the pulse amplitudes and maximum filter responses with the calibration lines. Simulated ^{129}I data were used to test and validate the analysis routines.

Besides ^{55}Fe containing absorbers with diameters of 680 µm prepared by drop deposition, tiny absorbers from the test chip, fabricated by KIT and ion-implanted by JGU, were carefully removed and glued on an aluminium absorber holder (see *Figure 12*). The absorbers were wire-bonded to the MMC sensors using 25 µm diameter gold wires. This procedure of connecting such small absorbers was demanding from an experimental point of view. To ensure that glue did not cover the whole absorbers and wedge bonding was still possible, only a very small amount of glue was placed below the absorbers. However, two of four absorbers were detached from the aluminium holder by bonding due to the spring force of the gold wires. The detector setup was as described in section 4.1.
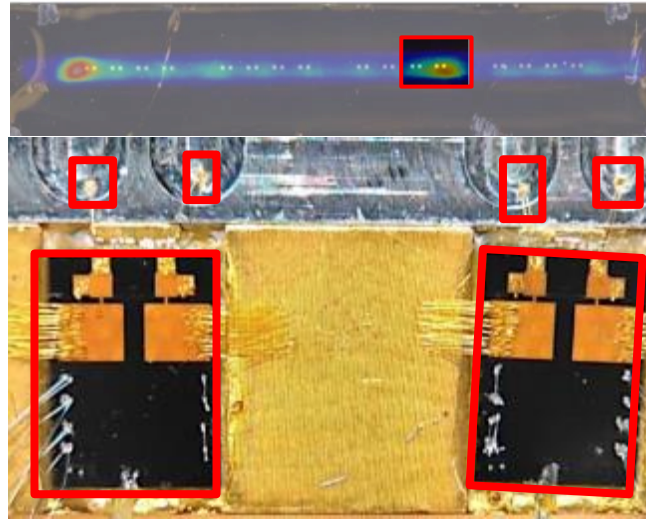
Figure 12: Top: The ion-implanted test chip overlayed with the activity distribution. The red box highlights the absorbers which were connected to the RoS-M MMCs. Bottom: Photography of a MMC setup with ion-implanted gold absorbers. The 170 µm × 170 µm × 24 µm microfabricated absorbers were glued on an aluminum holder and wire-bonded to the RoS-M MMCs using 25 µm in diameter gold wires.

Both spectra (*Figure 13*), the one caused by the EC decay of ^{55}Fe deposited by drop deposition (blue) and by ion-implantation (orange) are limited by suboptimal experimental conditions. The statistics are quite low with about 1.4×10^5 events (ion-implanted) and 3.2×10^6 events (drop deposited) in the part of the spectra above 400 eV. The same holds true for the energy resolutions of about E_{FWHM} = 39 eV (ion-implanted) and E_{FWHM} = 51 eV (drop deposited). While the Manganese K and L electron binding energy lines can clearly be observed, the M line is strongly superposed by noise fluctuations (*Figure 13* left). Low energy tailing due to energy loss in residuals created by drying of the activity containing aqueous solution, can be seen in spectra of the drop deposited sample. Since no solution is dispensed on the ion-implanted samples, this tailing does not occur in corresponding spectrum underlining the advantage of ion-implantation. Because of the low statistics, it seems unlikely to observe spectral structures caused by shake-up processes. However, as illustrated in *Figure 13* right, when applying dynamical binning, the high energy part (> 10 keV) of the observed spectra shows a similar slope as the theoretical predicted spectrum described in section 4.4. Similar to the theoretical model provided by UNL, the slope of the measured spectra could be due to the shake-off process after a capture of a K-electron. The preliminary measurements support the need for further high-statistics and high-quality measurements in order to study the shake processes involved in the EC of ^{55}Fe.
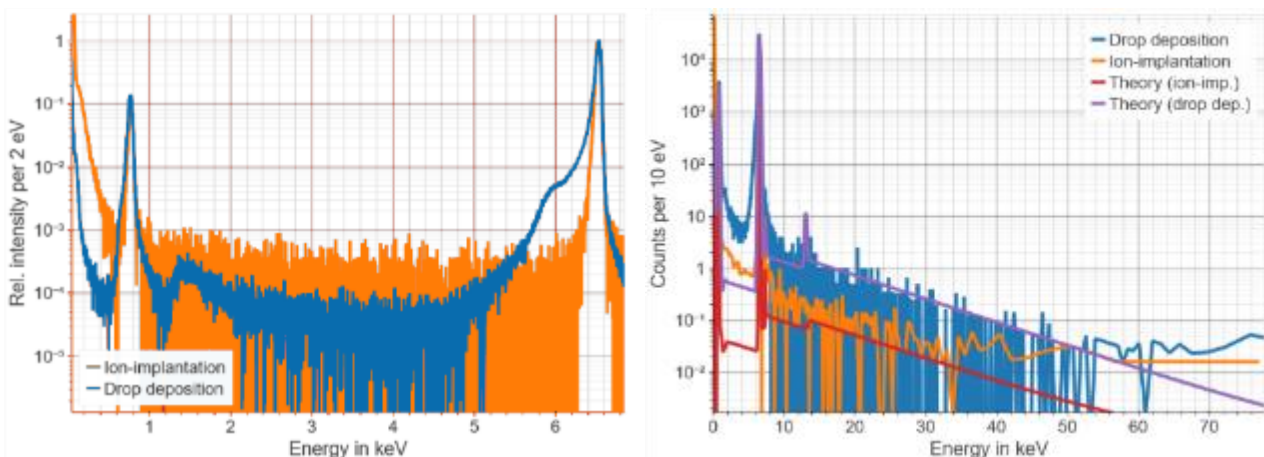

Figure 13: Comparison of the measured ^{55}Fe EC spectra of an ion-implanted source (orange) and drop deposited source (blue). Left: The dominant EC region up to the Manganese K binding energy of 6.5 keV is shown. Right: Additional to the measured spectra the theoretical prediction for the ion-implanted source (red) and drop deposited source (purple) are shown. The spectral shape above the Manganese K binding energy of the measured spectra and theoretical predictions are quite similar.

The measurement of the beta spectrum of [129]I is the result of a collaborative work between the partners. PTB provided to CEA a radioactive solution of [129]I without carrier, without impurities and with a relative high activity concentration. A challenging part of the measurement preparation was to embed a sufficient amount of activity in the absorbers, which was possible with the nanoporous silver (NPAg) layers developed by CNRS (see section 4.2). Finally, the absorbers were coupled with the MMCs developed by the KIT (see 4.1). The high quality of MMC production allowed to operate all of the 6 installed MMC chips in a single run without failure. Hence, a high statistics and multi-channel measurement was demonstrated. In addition, compared to reported measurements of the beta spectrum of [129]I, a high-energy resolution was achieved.

Monte Carlo simulations based on the Geant4 and Penelope frameworks were performed to define the dimension of the gold absorbers. For a target detection efficiency of 99.9%, the absorber thickness was minimized. With such large efficiency, systematic errors on the extracted decay data were avoided. Each absorber had a thickness of about 300 μm and an area of (1.8×1.8) mm². Twelve absorbers were prepared by enclosing the NPAg layers containing [129]I in gold. The absorbers were thermally connected to the sensors of six RoS-L MMCs using gold bonding wires. Ten absorbers contained about 1 Bq of [129]I each and two absorbers were empty to monitor the background and the calibration photon spectrum. Indeed, an external photon source of [57]Co was used to calibrate the energy scale. The six MMC chips were assembled on the multi-channel set-up designed by CEA (see *Figure 14*) and assembled in two daisy chains, an innovative design proposed by the KIT to reduce the number of wires. For the first time in ionizing radiation metrology, 12 (>1) low temperature detectors were measuring a source at the same time to increase the counting statistics. The data were recorded during 10 days at 30 mK.
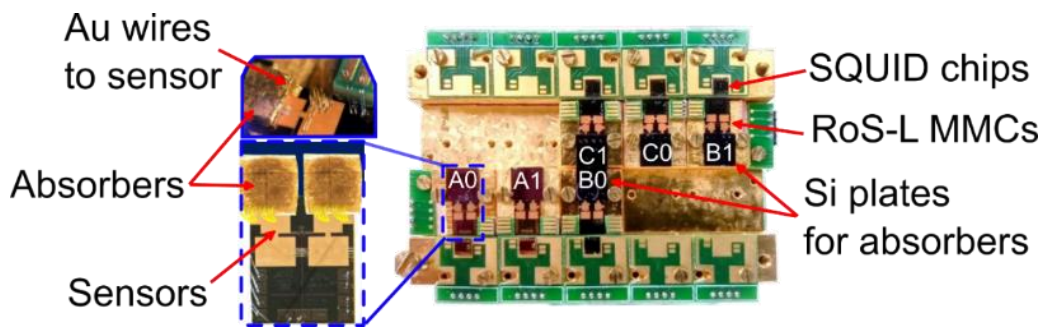

Figure 14: Photos of the multichannel MMC set-up used for the measurement of [129]I. The right picture shows the MMC chips (without the absorbers) with the label of the channels.
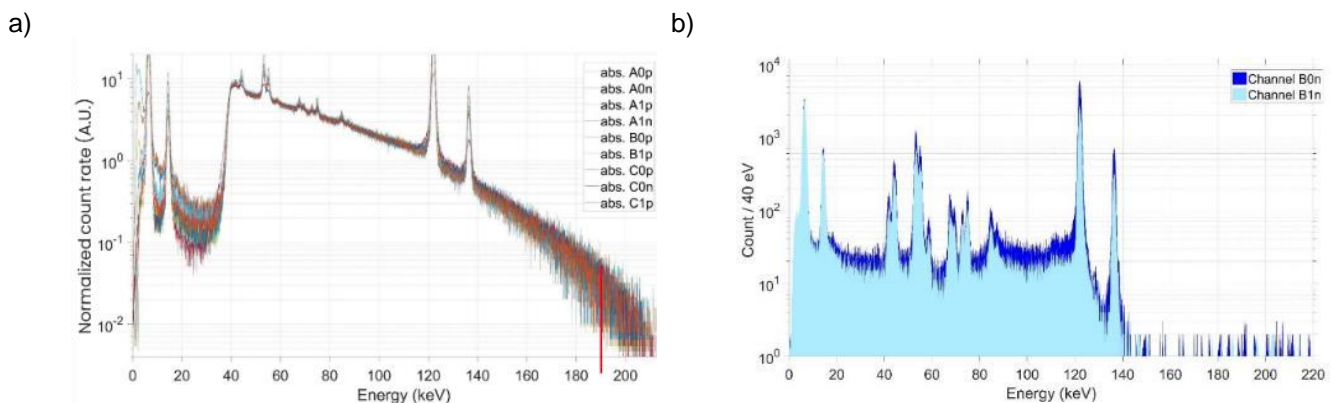

Figure 15: Energy spectra obtained from the multichannel MMC: a) Spectra from the 10 absorbers containing [129]I. b) Spectra from the two absorbers without [129]I showing the spectrum of [57]Co.

Error! Reference source not found. a) shows the 10 spectra from the absorbers containing an [129]I source. **Error! Reference source not found.** b) shows the spectra from the two empty absorbers dominated by [57]Co photons from the calibration source. The photon line at 122 keV from [57]Co was used as an energy calibration line, and the spectra of the 10 absorbers with [129]I were co-added. The resulting co-added spectrum (blue) is shown in *Figure 16* with intense calibration lines from [57]Co. These lines and the background are subtracted using the spectra obtained from the empty absorbers, giving the pink spectrum with a total of about 12×10^6

counts. The spectrum is similar to the expectation derived by Monte Carlo simulations, i.e. the beta spectrum corresponding to the beta emission to the excited state is shifted by 39.6 keV due to the emitted and measured internal conversion electron. Therefore, the beta spectrum of this beta branch was virtually measured with a 0 keV threshold. It is clearly observable that the measured end-point energy is much larger than the recommended value of 190.8 keV represented by a red vertical line. Until now, there is only one experimental value published in 1954. Compared to the published measurement, the present measurement demonstrated incomparable improvements in terms of resolution, detection efficiency, counting statistics and spectrum fidelity (no distortion). To verify that no distortion arose from the data analysis, simulated data based on experimental conditions were analyzed using the same routines. The output spectrum and related decay data were in agreement with the simulation's input. At PTB a preliminary spectrum analysis was performed to extract decay data with the help of the BetaShape code developed by CEA. As a result, a Q-value of 218(4) keV was determined as well as the preliminary decay probabilities determined to be 99.0(5)% for the decay to the excited state and 1.0(5)% to the ground sate, respectively. The determined branching ratios are in agreement with the evaluated values of 99.5(5)% and 0.5(5)%.
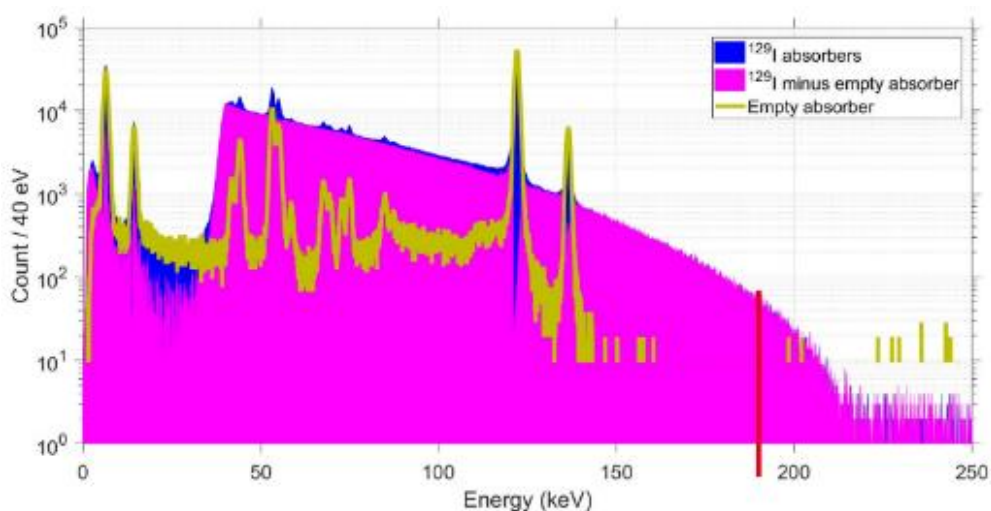

Figure 16: Co-added spectra of the 10 absorbers with ^{129}I, with (blue) and without (pink) the calibration lines (yellow). The red line at 190.8 keV corresponds to the position of the recommended end-point value.

Unfortunately, implanted sources of ^{55}Fe and sources of ^{129}I based on nanostructured silver became only available in the last months of the project. Therefore, the statistics and quality of the acquired spectra were not as high as aimed. Within the remaining time, only rough comparisons with the theoretical models were possible. The preliminary results however, showed the desired and promising direction. The preliminary measurements on ^{129}I indicated that the maximum beta energy is about 15% higher than currently adopted in literature. As a conclusion, the objective was not fully achieved.

4.4 Objective 4: Theoretical predictions of ^{129}I beta spectrum and ^{55}Fe electron-capture decay

In order to improve the model describing the decay of ^{55}Fe, a realistic model has been developed within the framework of the Relativistic Density Functional Theory (RDFT) by CNRS, in which a few exchange-correlation functionals and self-interaction-corrected models were implemented. These implemented models are among the most popular in the atomic physics community. A set of parameters fulfilling some physical constraints, namely limits of binding energies of inner subshells and an asymptotic behaviour of the effective potential, was determined by using the optimized effective potential method originally developed by Krieger, Li and Iafrate (KLI). It turns out that within this model, electron correlation effects seemed to play only a minor role on the electron capture process. This observation was confirmed by comparing the predictions for the EC decay of ^{7}Be with Multiconfiguration Dirac-Fock (MCDF) calculations performed by UNL with and without electron correlations. Only differences of a few percent were determined confirming the previous statement, also by considering that this effect should be most significant for low-mass nuclei.

The total shaking probabilities (which contribute to the total electron-capture probability) in both photoionization and electron capture processes were calculated by CEA using the Frozen Orbital (FO) and Daughter Excited (DE) approximations, respectively. Due to a lack of measured values, the results of the KLI and MCDF calculations were compared to predictions available in the literature, all established within nonrelativistic frameworks. The KLI and MCDF calculation results were in good agreement between each other as well as for photoionization and for electron capture, and also with available predictions. The used relativistic approach made us confident in predicting realistic shaking probabilities for medium and high-Z nuclei.

In addition, a large set of level energies and transition rates were calculated by UNL, both radiative and radiationless, for the Fe isonuclear sequence. These calculations were performed using the MCDF formalism. Given the enormous number of transitions (around $7 \cdot 10^6$) that was computed, an in-house code was built making use of standard parallelization tools to reduce computing times. Within this project, the K- and L-shell Fluorescence Yields (FY) of the complete Fe isonuclear sequence were computed for the first time from first principles. It was shown for the K-shell that the removal of the valence electrons resulted in a very small variation of the FY. For the L-shell, the behaviour was quite different from the one observed in other works for Cu ions where the average L-shell fluorescence yield was found to be very similar up to the removal of six M-shell electrons.

The electron capture model of BetaShape was adapted by CEA in order to consistently use the binding energies, wave functions and electronic configurations from the KLI and MCDF approaches, from CNRS and UNL respectively. It allowed to precisely include the hole effect on the other orbitals due to the vacancy created by the capture process, while this effect is accounted for approximately with the BetaShape atomic modelling. The electron capture probabilities determined by CEA with the KLI atomic model from CNRS were used together with the atomic parameters from the MCDF approach of UNL to determine the main component of the ^{55}Fe spectrum. For K captures, 63 energy levels are possible while for L captures, 243 levels are possible for the excited ^{55}Mn daughter atom. Moreover, in order to theoretically determine the width of each level, every electronic transition of one-vacancy levels (radiative) and between two- and one- vacancy levels (Auger electrons) needed to be computed. Therefore, the complete description of the atomic parameters for the electron capture decay of ^{55}Fe involved the calculation of 38 871 radiative transitions and around 350 000 Auger transitions. *Figure 17* shows the *ab initio* calculation of a K peak in a 4π measurement. It is composed of 63 Lorentzian distributions (one for each energy level) with widths corresponding to the initial excited level width (after a K capture). Each energy was computed assuming the final atomic system to be the ground state of the ^{55}Mn daughter atom. The relative intensity of each Lorentzian distribution is purely statics and only depends on the degeneracy of each level. The width of each excited level is almost equal, about 1.5 eV, and for some levels, the energy spread between levels is higher than its width (compare to *Figure 17* left). By assuming a Gaussian detector response with an energy resolution of 10 eV FWHM, the structures are no longer visible (*Figure 17* right). The available spectra (*Figure 13*) cannot be used to test the constraints of the theoretical model precisely. In case of the measurement using the ion-implanted sample, the statistics is too low to enable the observation of any shake processes as shown in *Figure 13* right in orange (measurement) and red (prediction). The prediction considers the most dominant shake processes after K electron and L electron captures. Namely, the K shake up and L shake up processes as well as the K shake off, L1 shake off and M1 shake off processes. The K, L and M capture probabilities are taken from DDEP. Due to the low statistics none of the shake-up processes can be observed. The decaying slope of the K capture shake-off process could be visible but needs to be confirmed with a measurement of a high-quality spectra.
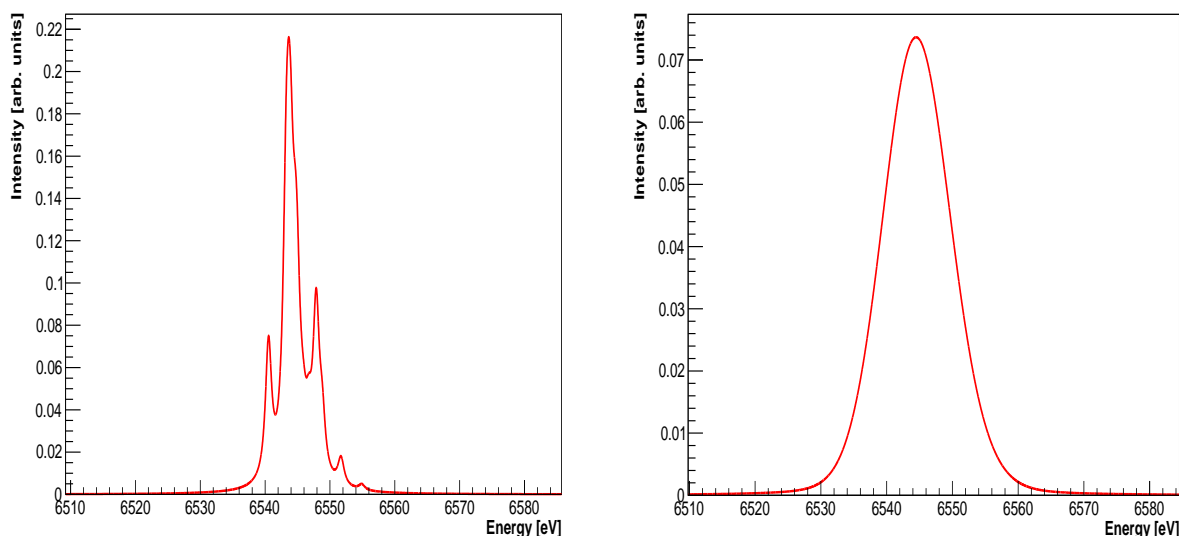
Figure 17: ^{55}Fe ab initio theoretical K spectrum of a 4π measurement (left) and convoluted with a Gaussian distribution with 10 eV FWHM (right).

Improving the theoretical description of ^{129}I beta spectrum required precise inclusion of nuclear structure information determined with an accurate model. Two models were considered in this project.

The first one is the self-consistent Hartree-Fock-Bogoliubov (HFP) approach with Quasiparticle Random Phase Approximation (QRPA) and is, in principle, more accurate. However, it requires large-scale calculations on supercomputers. It was originally developed by CEA in cylindrical coordinates to account for nucleus deformation, an important feature for accurate predictions. The main, underestimated challenge in this project was to adapt this formalism to determine the one-body transition densities (OBTD) in the spherical formalism of Behrens and Bühring required by the beta decay code of CEA.

The first step was to fully derive all the equations that allow transforming the (HFB+QRPA) results from cylindrical coordinates to spherical coordinates. Beyond the mathematical difficulty, the choice of the spherical basis is of high importance not to lose accuracy in the description of nucleus deformation. The second step was to understand how to establish OBTD, which are shell model quantities, from (HFB+QRPA) results, which employs a particle-hole description. Both steps were done in close collaboration between CEA and IPSA. The beta decay code of CEA was then adapted in order to be able to use the (HFB+QRPA) predictions. Next, the beta decay calculation with (HBF+QRPA) structure was tested focusing on a simple case, the pure Gamow-Teller allowed ^{6}He transition. For validation, nuclear structure calculations within the shell model were performed by CEA with the NushellX code. Theoretical half-lives were determined from beta spectrum integration. The different nuclear matrix elements involved in ^{6}He decay were studied in detail and a sensitivity study to an effective value of the axial-vector weak interaction coupling constant was performed. As a conclusion, the whole approach was validated and the difference between shell model and (HFB+QRPA) predictions was identified to be due to the limitations of the latter model at small masses.

CEA and IPSA then focused on ^{129}I second forbidden non-unique decay. The particle-hole configurations in the nuclear states involved were analysed and those that mostly contribute were selected. The first excited state of ^{129}Xe is predicted at 60 keV, compared to the experimental value of 39.578 (2) keV, which is an exceptional accuracy for a nuclear structure model. All the data that describe these nuclear states, which include nucleus deformation, were produced. The full calculation and identification of the beta spectrum of ^{129}I decay with these (HFB+QRPA) predictions still has to be achieved. The large total angular momentum change is anticipated to induce a very large number of OBTD, especially if a full basis is considered. Computational burden is therefore always an important challenge.

The bata decay of ^{129}I was also described within the spherical shell-model framework. Calculations were performed by CEA with the NushellX code in order to determine the OBTD. One of the advantages of this nuclear structure code is that it comes with effectives Hamiltonians adjusted on experimental data. The *jj55pn* model space and the *sn100pn* interaction were used: ^{129}I and ^{129}Xe nuclear states are then described by a fixed ^{100}Sn core and a valence space containing 4 protons and 26 neutrons. Several attempts were necessary to constrain as less as possible the valence space but keeping a tractable computational burden. Influence of these calculations on the predicted beta spectrum was studied considering two extreme cases: a very

constrained valence space, and an almost no constrained valence space. The number of OBTD to determine was consequent due to the large total angular momentum change in ^{129}I decay.

In addition, influence of other components was studied. First, the modelling of the atomic exchange effect, originally established only for the allowed transitions, was extended by CEA to the forbidden unique decays. It was demonstrated that the allowed exchange correction applied to the Fermi function was a good approximation for the forbidden unique transitions. To disseminate the results, they were included in the BetaShape code of CEA thanks to an extensive tabulation of the correction factors. In order to ensure accurate predictions at very low energy, the screening effect in the BetaShape modelling was also revised by tabulating the correction factors on the Fermi function and the I_k parameters. Since then, new developments have been carried out and implemented for a specific calculation of the atomic exchange effect in forbidden non-unique beta transitions. Full calculations requiring the convolution of the atomic and nuclear matrix elements have been performed for the second forbidden non-unique transitions of ^{99}Tc and ^{129}I decay with the BetaShape wave functions. No significant change was noticed compared with the "forbidden unique approximation" treatment.

Related to inclusion of nuclear structure in beta decay calculations, the influence of the Conserved Vector Current (CVC) hypothesis was studied. In forbidden non-unique decays, the dominant matrix element is a relativistic vector matrix element, which cannot be accurately determined from the usual, most common non-relativistic nuclear structure models. The CVC assumption provides relationships between relativistic and non-relativistic vector matrix elements, helping a lot in estimating correctly this matrix element. Application of CVC requires introducing the Coulomb displacement energy in the decay, which was calculated under various assumptions of different accuracies. Eventually, the influence on the spectrum shape of an effective value of the axial-vector coupling constant g_A of the weak interaction was also studied. *Figure 18* illustrates the influence of the nuclear structure modelling and of the effective value of g_A on the beta spectrum of ^{129}I decay. Calculations were performed with the latest recommended Q-value.
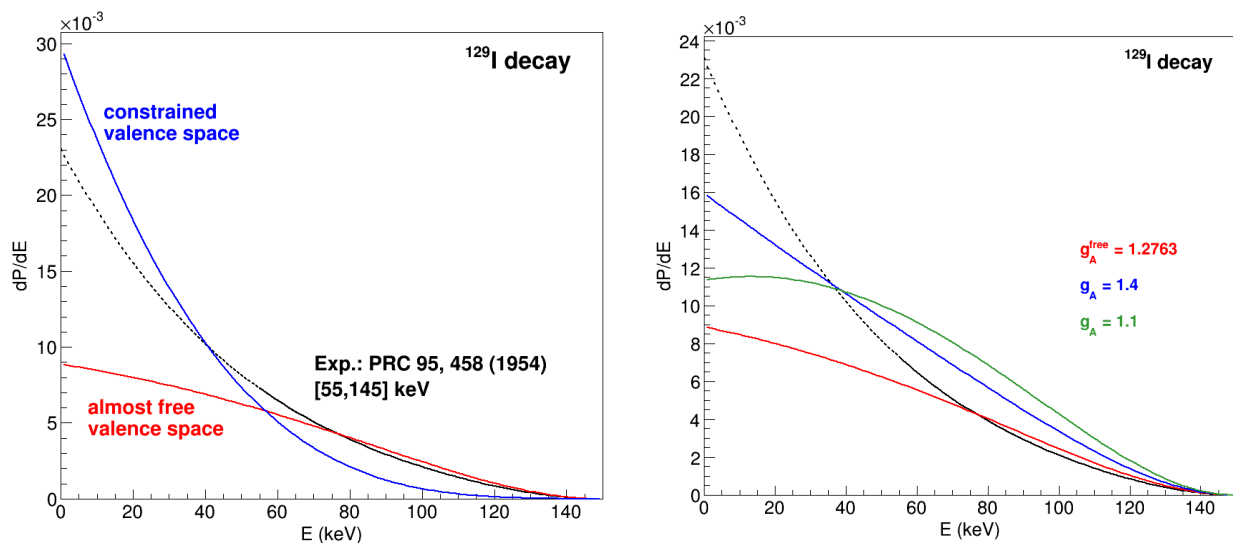

Figure 18: Left: Influence of the nuclear structure modelling on the beta spectrum of ^{129}I decay. Right: Influence of the axial vector coupling constant g_A on the beta spectrum of ^{129}I decay, with the almost not restricted valence space as a reference.

As it was shown for ^{151}Sm (see Deliverable 4), MMC measurements can also be used to extract decay probabilities of competing beta branches, which are very fundamental decay data. The same procedure as used for ^{151}Sm can also be applied to ^{129}I. Theoretical calculations were performed with a preliminary extraction of the Q-value from MMC measurements, which was surprisingly found 15% higher than the recommended Q-value. A preliminary branching ratio analysis indicates that this can also be applied for ^{129}I as it is shown in *Figure 19*.
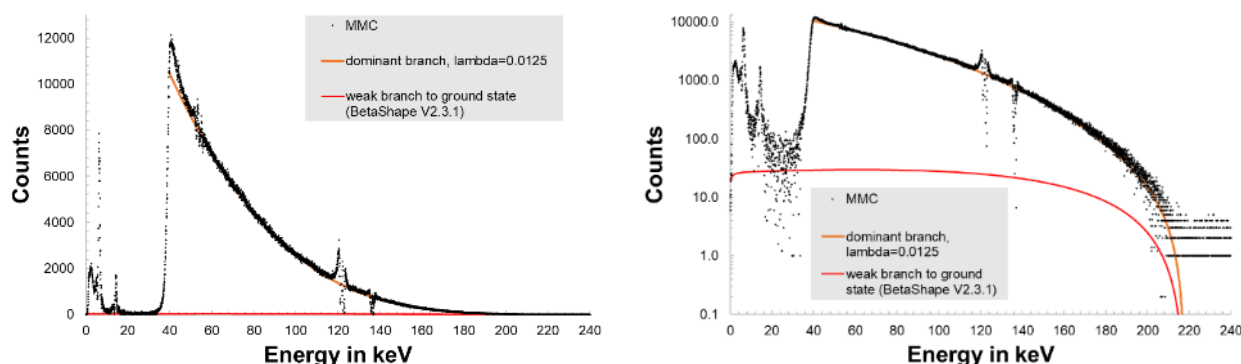
Figure 19: The ^{129}I MMC data were used to determine the decay probabilities of the two beta branches. The beta spectrum for the ground state transition was adjusted in the energy range from 20 keV to 30 keV and the dominant branch was adjusted in the range from 60 keV to 100 keV after subtracting the ground state component. The preliminary decay probabilities were determined to be 99.0(5)% and 1.0(5)%, respectively, and are in agreement with evaluated values (99.5(5)% and 0.5(5)%). Lower uncertainties are to be expected with optimized measurement and analysis techniques. The right figure shows the same plot with logarithmic ordinate.

To conclude, the theoretical predictions for ^{129}I and ^{55}Fe spectra could only be substantiated preliminary due to a lack of high-statistics measurements. Nevertheless, the models were applied on other nuclides including the EC-decaying ^{7}Be, and the beta-decaying nuclides ^{151}Sm, ^{99}Tc and ^{176}Lu. Hence, it can safely be stated that this objective was fully satisfied.

5 Impact

A web page (https://prima-ltd.net/) was set up to give interested parties an overview of the activities and scientific goals the consortium was addressing within the project. Contact details for interested parties were given and a stakeholder registration platform was established and advertised. A concept for keeping the stakeholders up to date was developed. Information about recent publications, conferences and training courses was disseminated using these platforms. In total 18 stakeholders from 15 organizations have registered. Two well-attended stakeholder workshops as well as two training courses were held. The stakeholder workshops covered all aspects of the project starting with a project overview followed by presentations of the work packages and discussions. In the two training courses, recent progress in nuclear counting using MMCs as well as in MMC measurements and analysis in metrology was presented. While the focus was set on the project, also external speakers were invited and contributed to the training courses. About 35 participants from universities, research institutes and national metrology institutes not involved in the project joined the training courses

In total, the project and its progresses were presented at several conferences with a total of 25 talks and posters. Outcomes of the project resulted in 11 open access, peer-reviewed publications. Six technical visits – two of them virtual – took place within the consortium for in-depth discussion on specific technical aspects.

Impact on industrial and other user communities

Many users of radioactive materials will benefit from improved nuclear decay data and related more accurate activity determination. The nuclear power industry uses decay data to determine the residual heat and its evolution with time in nuclear reactors and in nuclear waste management. For example, the average energy per ^{129}I decay depends on the shape of the beta spectrum and the maximum beta energy. Thanks to the project, this data will be available with significantly improved accuracy. The preliminary experimental results of the maximum beta energy of ^{129}I suggests a higher value, which will be of enormous importance. Results of environmental monitoring of radioactivity will also be able to reduce uncertainties by using decay data with smaller uncertainties.

Nuclear medicine will also benefit because, for example, the improved beta spectrum calculation methods from this project can be used. This plays a role in some radiopharmaceuticals that can be used for diagnosis or therapy. More accurate decay data allow a more accurate calculation of the dose per administered activity, whose determination will also become more accurate with the results of this project.

While the nuclides investigated in this project are not of specific interest in industry or medicine, the newly developed and validated theoretical models covered nuclides in these applications. Experience from previous projects prove that newly available nuclide data are taken up by NMIs/DIs soon resulting in a better service and better-quality radioactive sources for commercial customers.

Impact on the metrology and scientific communities

The development of a completely new method for primary activity determination will be a great benefit for radionuclide metrology, since it will lower the achievable uncertainties by up to an order of magnitude. Some nuclides, such as ^{7}Be, that have not been standardised yet might also be accessible with this method.

Advanced theoretical calculations of decay spectra and their validation with high-resolution and high-statistics data of the ^{55}Fe electron capture and ^{129}I beta decay down to lowest energies, will benefit the accuracy of decay data in general. This decay data, based on the broadly applicable theoretical models, is not only used in metrology, but, for example, also in the calculation of neutrino spectra, especially from nuclear reactors for the determination of neutrino oscillation parameters or the search of non-weak interacting (sterile) neutrinos. Background estimation of low-background experiments, such as the search for dark matter reaching beyond the standard model of particle physics, also rely on accurate decay data. It should be noted again that the preliminary experimental results of the maximum beta energy of ^{129}I show unexpected deviations, which will be of high importance for metrology and other fields.

A paper on the study of the beta spectra and decay scheme parameters of ^{151}Sm has been published and the article was already cited by other researchers and it triggered new proposals for verification experiments to determine the maximum beta energy by means of Penning traps. Corresponding information for public relation purposes (https://www.ptb.de/cms/service-seiten/news/newsdetails.html) has also been published as an early outcome of the work carried out in the framework of objective 4. The developments in MMC technology, from fabrication to data acquisition and data processing of multi-channel spectrometers, will also not only benefit the contributing partners, but also the LTD community as whole.

Another paper, that has recently been published, presents the K- and L- shell fluorescence yield values of the full isonuclear sequence of Fe ions, using a state-of-the-art multiconfiguration Dirac–Fock approach.

Representatives of CEA, PTB and KIT took part in a technical meeting of the AMoRE Double Beta Decay Experiment. This experiment also employs MMC detector technology. The PrimA-LTD representatives informed specifically about the detector technology developed within the project (obj. 1) as well as MMC readout strategies (obj. 3) as an early outcome.

Impact on relevant standards

The project led to improved nuclear decay data by direct measurements and by improving the theoretical calculation techniques. Hence, the outcome of this project is a valuable contribution for nuclear decay data evaluations. Publications and tables with recommended data play a key role for research and many applications and are also a basis for international standards. Presentations were given during each EURAMET TC-IR meeting highlighting the research activities, presenting the latest developments and the projected output. The uptake of new decay data (obj. 4) and awareness for the importance of decay data for activity determination (obj. 3 and 4) are proof of the early impact from this project. Results of the high-precision measurements on ^{151}Sm have already been incorporated into an evaluation of the Decay Data Evaluation Project (DDEP) and results are publicly available (http://www.lnhb.fr/nuclides/Sm-151_tables.pdf and http://www.lnhb.fr/nuclides/Sm-151.BetaShape.zip).

Longer-term economic, social and environmental impacts

The wider dissemination of MMCs and similar LTD technologies can and will have large impact on research, medicine and industry. In X-ray spectrometry, LTDs can combine high resolution and high energy bandwidth, that classically require two different detector systems. Nuclear forensics and nuclear safeguards can be made more accessible, since the high resolution of LTDs allows radiochemical preparations before measurements to be omitted and can combine the capabilities usually obtained separately from alpha- and mass-spectrometry in a single measurement.

The use and benefits in nuclear power industry, environmental monitoring and nuclear medicine, will also continue in the long-term, both from the improved decay data and better activity standardisation with the inevitable wider adoption of LTD technology. All these end-users base their developments on nuclear decay data that come either from the DDEP (Decay Data Evaluation Project) collaboration, designed for and coordinated by the metrology community, or from the ENSDF (Evaluated Nuclear Structure Data File)

community. Both have adopted the BetaShape code, which has been significantly improved in this project, for their evaluations, ensuring significant knowledge transfer from this project to the most applicative communities (obj. 4).

6   List of publications

1. Kossert, K., Loidl, M., Mougeot, X., Paulsen, M., Ranitzsch, P., Rodrigues, M.: High precision measurement of the ^{151}Sm beta decay by means of a metallic magnetic calorimeter. In: Applied Radiation and Isotopes 185 (2022), 110237, https://doi.org/10.1016/j.apradiso.2022.110237

2. Pinheiro, D., Fernandes, A., Godinho, C., Machado, J, Baptista, G., Grilo, F., Sustelo, L., Sampaio, J.M., Amaro, P., Leitão, R.G., Marques, J.P., Parente, F., Indelicato, P., de Avillez, M., Santos, J.P., Guerra, M.: K- and L-shell theoretical fluorescence yields for the Fe isonuclear sequence. In: Radiation Physics and Chemistry A 203 (2022), 110594, https://doi.org/10.1016/j.radphyschem.2022.110594

3. Quarati, F.G.A., Bollen, G., Dorenbos, P., Eibach, M., Gulyuz, K., Hamaker, A., Izzo, C., Keblbeck, D.K., Mougeot, X., Puentes, D., Redshaw, M., Ringle, R., Sandler, R., Surbrook, J., Yandow, I.: Measurements and computational analysis of the natural decay of ^{176}Lu. In: Physical Review C 107 (2023), 024313, https://arxiv.org/abs/2207.14195

4. Agnes, P. et al.: Search for low-mass dark matter WIMPs with 12 ton-day exposure of DarkSide-50. In: Physical Review D 107 (2023), 063001, https://doi.org/10.1103/PhysRevD.107.063001

5. Turkat, S., Mougeot, X., Singh, B., Zuber, K: Systematics of log ft values for $\beta-$, and EC/β+ transitions. In: Atomic Data and Nuclear Data Tables 152 (2023), 101584, https://doi.org/10.1016/j.adt.2023.101584

6. Hadid, J., Rodrigues, M., Harouri, A., Dupuis, C., Bouville, D., Martin, A., Loidl, M., Ferlazzo, L.: Detachable three-layer Au absorber microfabrication for low-temperature detectors. In: Micro and Nano Engineering 20 (2023), 100220, https://doi.org/10.1016/j.mne.2023.100220

7. Mougeot, X.: Atomic exchange correction in forbidden unique beta transitions. In: Applied Radiation and Isotopes 201 (2023), 111018, https://doi.org/10.1016/j.apradiso.2023.111018

8. Andoche, A., Mouawad, L., Hervieux, P.-A., Mougeot, X., Machado, J., Santos, J.P.: Influence of atomic modeling on electron capture and shaking processes. In: Physical Review A 109 (2024), 032826, https://doi.org/10.1103/PhysRevA.109.032826

9. Paulsen, M. et al.: High precision measurement of the ^{99}Tc β spectrum, Physical Review C, [submitted]; Preprint available: http://arxiv.org/abs/2309.14014

10. Müller, M., Rodrigues, M., Beyer, J., Loidl, M., Kempf, S.: Magnetic Microcalorimeters for Primary Activity Standardization Within the EMPIR Project PrimA-LTD, Journal of Low Temperature Physics 214 (2024), https://doi.org/10.1007/s10909-024-03048-7

This list is also available here: https://www.euramet.org/repository/research-publications-repository-link